Real-time high-temperature scanning indentation: Probing physical changes in thin-film metallic glasses

Solene Comby-Dassonneville, Gabrielle Tiphene, Alejandro Borroto, Gaylord Guillonneau, Lucian Roiban, Guillaume Kermouche, Jean-François Pierson, Jean-Luc Loubet, Philippe Steyer

Real-time high-temperature scanning indentation: Probing physical changes in thin-film metallic glasses

Solène Comby-Dassonneville[1], Gabrielle Tiphéne[2,3], Alejandro Borroto[4], Gaylord Guillonneau[2], Lucian Roiban[1], Guillaume Kermouche[3], Jean-François Pierson[4], Jean-Luc Loubet[2], Philippe Steyer[1]

[1] *Université de Lyon, INSA Lyon, UCBL, CNRS, MATEIS, UMR 5510, 69621 Villeurbanne, France*

[2] *Université de Lyon, Ecole Centrale de Lyon, LTDS, UMR CNRS 5513, 36 avenue Guy de Collongue, 69134 Ecully, France*

[3] *Mines Saint-Etienne, CNRS, UMR 5307 LGF, Centre SMS, 42023 Saint Etienne, France*

[4] *Université de Lorraine, CNRS, IJL, UMR 7198, F-54000 Nancy, France*

Corresponding author : Philippe Steyer, philippe.steyer@insa-lyon.fr , 7 avenue Jean Capelle 69621 Villeurbanne Cedex, France

Highlights

- HTSI is a new method to measure thermally activated mechanisms in TFMGs
- Real-time monitoring of physical changes in ZrCu TFMGs was performed
- The temperature dependence of mechanical properties was obtained in one batch
- Transition temperatures and kinetic information were successfully accessed
- Toward measuring local transitions as a function of sample length-scale

Keywords

Metallic glass; *in situ* high-temperature nanoindentation; thin films; crystallization; glass transition

Abstract

This work reports the use of a new high-temperature scanning indentation (HTSI) technique to monitor the physical changes occurring in thin-film metallic glasses (TFMGs) *in situ* during heat treatment at the local scale. Using this technique, based on high-speed nanoindentation performed during thermal cycles, the entire mechanical evolution with temperature of a binary model ZrCu TFMG was characterized in only a few hours. This approach enabled clear identification of the physical evolutions of the amorphous coatings in only one indentation experiment, highlighting in particular the metallic glass-to-supercooled liquid transition and crystallization process. In addition, the brittle-to-ductile transition was precisely characterized, with remarkable agreement with the literature. Moreover, the mechanical response of the ZrCu thin film was assessed *in situ* throughout the entire supercooled liquid stage, providing key kinetic information. Nanohardness measurements also enabled the crystallization fraction to be computed over time during the crystallization process. In addition, differential scanning calorimetry and high-temperature X-ray diffraction were performed for comparison purposes, with excellent agreement with the HTSI results. Through this model out-of-equilibrium thin-film study, both the efficiency and robustness of HTSI were demonstrated, providing a better understanding of the thermally activated mechanisms of small-scale systems.

1. Introduction

Bulk metallic glasses (BMGs) were discovered in the 1960's [1]. They consist of metallic alloys in an amorphous state, resulting from a fast solidification from the liquid alloy. In this out-of-equilibrium state, the atomic structure of the alloy is frozen without undergoing crystallization. Thus, metallic glasses are characterized by the absence of crystallographic defects and a global intrinsic chemical homogeneity. This structure gives them exceptional properties, including outstanding mechanical and magnetic properties, super-formability at high temperature, and high corrosion resistance [2-8]. These characteristics make them excellent candidates for use in various fields, including the sport and luxury industries [8-10] and biomedical applications [11-15].

The astonishing mechanical properties of BMGs have been extensively studied in the literature [16-19]. In particular, BMGs exhibit high yield strength at room temperature, close to the theoretical limit, with Young's moduli of the same order of magnitude as that of their crystalline counterparts, resulting in a high maximal elastic strain of approximately 2%. However, BMGs are generally not capable of work-hardening, inducing sharply localized deformation into shear bands, which is responsible for catastrophic failures. In the past two decades, this limitation has been overcome by incorporating heterogeneities, such as crystalline phases in metallic glass/crystalline composites [20-22] or glass/glass interphases [23], in BMGs. This leads to easier and more homogeneous nucleation of shear bands as well as continuous multiplication of the shear bands during deformation, further extending the numerous potential fields of applications for metallic glasses.

Nevertheless, the applications of BMGs remain limited by the fast quenching (typically current rates from 10^2–10^3 K s^{-1} for bulk pieces to 10^5–10^6 K s^{-1} for ribbons) necessary to limit the crystallization during the manufacturing process. As a result, only small pieces of multicomponent materials can be obtained in the bulk state. As an alternative, condensation from the vapor phase to form a solid film using physical vapor deposition (PVD) is another way to design metallic glasses. PVD is inherently associated with very high quenching rates (10^6–10^9 K/s) [24]. As a result, large surfaces of thin-film metallic glasses (TFMGs) can be obtained. Thanks to this rapid cooling rate, a large range of chemical compositions can also be accessed in the metallic glass state, allowing the physical study of model binary systems [25, 26]. However, because of the thin-film nature of the obtained metallic glass, dedicated characterization techniques, which are well adapted to small-scale systems, must be used for the characterization of TFMGs.

Nanoindentation is undoubtedly the technique of choice to measure the mechanical properties of thin films. Nanoindentation testing was specifically developed to study small-scale materials, such as thin films [27-30], as it allows control of the indentation depths to as little as tens of nanometers, with nanometer-scale sensitivity. This was a technological breakthrough compared with previous hardness or microhardness tests such the well-known Brinell, Vickers, and Rockwell tests. In addition, the direct monitoring of both the load applied to the sample and the indentation depth of the sample during indentation allow both the hardness and

Young's modulus to be determined without any imaging technique, thanks to the elastic analysis of the unloading part of the indentation curve [27, 31-33]. With the development of the continuous stiffness measurement (CSM) mode in nanoindentation, the mechanical properties can also be continuously measured as a function of depth during the entire loading segment of the nanoindentation test [32, 34].

Thus, benefitting from the numerous advantages of this technique, including its precision and ease of use and the wealth of data provided by these tests [35-37], TFMGs have been extensively tested using nanoindentation at room temperature over the past two decades [38-43].

However, because of their out-of-equilibrium nature, the mechanical properties of metallic glasses are strongly temperature dependent. In particular, they are deeply affected by thermally activated mechanisms, such as structural relaxation, glass transition, or crystallization [8, 18, 44, 45]. For BMGs, these transitions are usually investigated using differential scanning calorimetry methods (DSC), dynamic mechanical analysis (DMA), thermomechanical analysis (TMA), or even high-temperature X-ray diffraction (HT-XRD) [8, 9, 46-48] as well as by tensile or compression tests at high temperature [10, 17, 49-53]. However, although these methods are well suited for BMGs, it is difficult to adapt them to small-scale systems such as thin films.

Recently, strong improvements have been made in high-temperature nanoindentation, providing access to hardness, Young's modulus, and creep properties at temperatures as high as 1373 K [54-57]. These developments have opened the way to study thermally activated mechanisms [58, 59]. However, the time-scale of standard continuous stiffness measurement (CSM) nanoindentation does not allow the precise monitoring of these mechanisms. Very recently, a new technique, high-temperature scanning indentation (HTSI), has been developed. It is based on very fast indentation applied during a thermal cycle [60]. This technique is able to overcome the limitations of CSM nanoindentation associated with thermal drift during non-isothermal cycles, allowing the real-time monitoring of recrystallization in cold-rolled pure aluminum alloy during heating. Benefitting from this technique, it is now possible to use nanoindentation as a local probe to access thermally activated physical changes within a material. In this context, HTSI appears to be a

key technique to study the mechanical properties of TFMGs at high temperature and to link these properties with the thermally induced physical changes occurring within the material.

Herein, we report the first real-time observations of physical changes occurring within a TFMG during a thermal cycle and assessed by HTSI. For this purpose, HTSI measurements were performed on model binary ZrCu TFMGs, and the different transitions occurring within the coatings (*i.e.* metallic glass-to-supercooled liquid transition and crystallization) are discussed in light of hardness and strain-rate sensitivity responses. The HTSI results are also compared with those obtained using conventional techniques, including differential scanning calorimetry (DSC) and high-temperature X-ray diffraction (HT-XRD).

2. Experimental

2.1 Film synthesis

ZrCu thin-film metallic glasses were deposited using DC magnetron co-sputtering of Zr and Cu metallic targets in the presence of argon. The sputtering chamber was pumped down via mechanical and turbo-molecular pumps, resulting in a base vacuum of 10^{-6} Pa. To ensure good lateral homogeneity of the film composition and thickness, the depositions were performed with the substrate holder in rotation mode. The cathodes were mounted in a confocal configuration, and the target-to-substrate distance was fixed at 9 cm. An argon flow rate of 30 sccm and a working argon pressure of 0.5 Pa were used. Zirconium and copper targets (50.8-mm diameter, 3-mm-thick, and purity higher than 99.9%) were powered by a Maxim 1000 DC generator. Under these conditions, ZrCu thin films with a Cu content of 50 at% were obtained by applying discharge currents of 0.3 A to the Zr target and 0.056 A to the Cu target. The films were deposited without external heating.

The thin films were deposited onto different substrates, depending on the characterization technique. For the nanoindentation, X-ray diffraction (XRD), and scanning electron microscopy (SEM), 6-µm-thick ZrCu TFMGs were deposited onto fused silica and silicon substrates during the same deposition batch. The soft film on hard substrate configuration, together with the thickness of the deposited film ensure a limited contribution of the substrate on hardness measurements during indentation [61, 62] (Fig. S1).

In addition, samples for differential scanning calorimetry (DSC) measurements were deposited onto sodium chloride substrates, ensuring 5 mg of material for each sample. Substrate-free samples for DSC were then easily obtained by dissolving the NaCl substrate in distilled water. Furthermore, a 70-nm thin film was deposited onto a dedicated Nano-Chip from DENS solutions for transmission electron microscopy (TEM) observations [63].

2.2 High-temperature scanning indentation

High-temperature scanning indentation (HTSI) tests were conducted on ZrCu TFMGs to assess the evolution of their mechanical behavior with temperature. This new technique is based on high-speed nanoindentation performed during thermal cycles [60].

HTSI tests were performed using an InSEM HT nanoindentation system (KLA Nanomechanics) and a Berkovich sapphire tip. The measurements were conducted in a VEGA3 scanning electron microscope (Tescan), ensuring a 10^{-3} Pa vacuum. For high-temperature measurements, the tip and sample were independently heated by conduction. The tip and sample temperatures were measured by thermocouples on the backside of the fused silica substrate and ahead of the indentation tip and were independently controlled by specific proportional–integral–derivative (PID) loops. The tip and sample temperatures were calibrated to perfectly match those during isothermal tests using the method described by Minnert et al. [57]. The temperature offsets observed during these calibration steps were then extrapolated to adjust temperatures during the heating ramp, ensuring good agreement between the sample and tip temperatures during the entire thermal cycle.

HTSI requires high-speed nanoindentation tests to limit drift issues during measurements. It is thus not compatible with the standard CSM indentation methods, as their duration is longer than 1 min and thus requires a temperature stabilization time of several hours. The method for high-speed nanoindentation is fully described in [60]. It is based on a quarter sinus loading up to 25 mN with a 0.5-s loading time. This step is followed by a 0.1-s holding step at maximal load for creep measurements. A 3-step unloading is

finally performed for stiffness computation, with 3 unloading steps at 0.75, 0.5, and 0.25 of the maximal load. A schematic illustration of the resulting loading curve is presented in Fig. 1a.

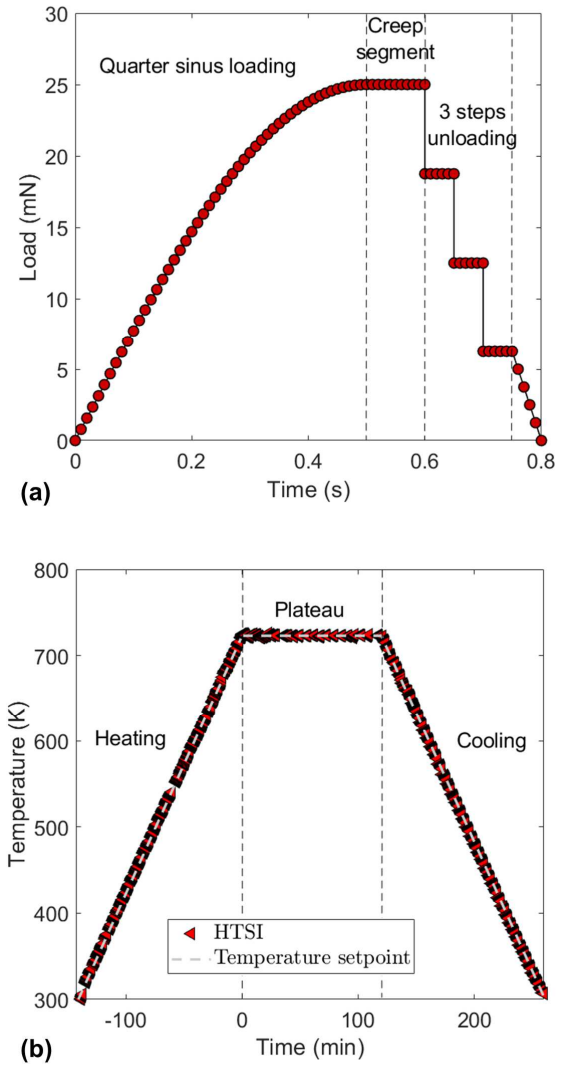

FIG. 1: (a) Schematic illustration of the loading versus time curve during HTSI, involving a quarter sinus loading up to a maximal load, a creep segment at maximal load, and a 3-step unloading at 0.75, 0.5, and 0.25 of the maximal load for stiffness computation. (b) Sample temperature during HTSI. The data points correspond to the temperature during each individual nanoindentation test. The dotted line corresponds to the temperature set-point during the thermal cycle.

HTSI tests were conducted on ZrCu TFMGs during an entire thermal cycle, including a heating step from 293 K to 723 K at 3 K min^{-1}, a 2-h plateau at 723 K, and a cooling step from 723 K to 293 K at –3 K min^{-1} (Fig. 1b). For comparison purposes, when studying the serrations events on the loading curves,

nanoindentation testing was also performed during the isothermal plateau at 298 K, 473 K, 573 K, 623 K, and 673 K. For these tests, the previously described high-speed nanoindentation as well as the standard CSM method with a 0.05 s^{-1} indentation strain rate were used.

2.3 XRD characterization

The crystallographic structure of films before and after HTSI was investigated using XRD using an AXS Bruker D8 Advance diffractometer with Cu K_α radiation (λ = 0.15406 nm) in Bragg–Brentano geometry. For comparison with high-temperature nanoindentation testing, the thermal stability of ZrCu TFMGs was also investigated using *in situ* high-temperature XRD (HT-XRD) in an Anton Paar HTK 1200 oven chamber operating under vacuum (10^{-3} Pa). XRD measurements were performed with a locked coupled scan (2θ from 27° to 47°) during the same thermal cycle as for HTSI (heating up to 723 K with a 3 K min^{-1} equivalent rate, 2-h plateau at 723 K, and cooling down to room temperature at a −3 K min^{-1} equivalent rate).

For each XRD diffractogram, the crystallization fraction F_x was estimated using Eq. 1, where I_a and I_x correspond to the integrated intensities of the amorphous phase and crystallized phases, respectively, after deconvolution of each contribution from the total diffraction intensity [64, 65].

$$F_x = \frac{I_x}{I_a + I_x} \qquad \text{Eq. 1}$$

2.4 DSC measurements

The glass transition temperature (T_g) and the onset of crystallization temperature (T_x) were determined by differential scanning calorimetry (DSC) using a Perkin Elmer DSC-7 under high-purity dry nitrogen at a flow rate of 20 mL min^{-1}. Substrate-free samples of 5 mg each were heated from 303 K to 823 K at a constant heating rate of 3 or 15 K min^{-1}. The T_g and T_x values from the DSC measurements are given

in Table 1, and the corresponding curves are shown in Fig. S2. They are in good agreement with the values in the literature for similar composition [26, 42].

TABLE 1: Glass transition temperature (T_g) and onset of crystallization temperatures (T_x) obtained from DSC for two different heating rates.

	3 K min^{-1}	15 K min^{-1}
T_g	658 K	668 K
T_x	680 K	702 K

2.5 Microstructural characterization

Microstructural observations of the initial state of the ZrCu TFMGs were obtained by SEM using a field-emission gun from Zeiss (Supra 55 VP) as well as by TEM using a FEI-TITAN eTEM operating at 300 kV under high vacuum.

3 Methodology

HTSI gives access to contact stiffness measurements using the unloading part of the load–depth curve, which allows hardness computation. It also gives access to creep measurements using the creep segment at maximal load, which allows strain-rate sensitivity computation. The two independent analyses enabling hardness calculation, on the one hand, and strain-rate sensitivity determination, on the other hand, are described in this section.

3.1 Analysis of unloading part

The indentation tests were analyzed using Loubet's model [33, 66, 67], which is well-adapted for this system and material [60]. In particular, this model accounts for pile-up that can occur around the contact and increase the contact area, leading to hardness overestimation if not considered. According to Loubet's model, the contact depth h_c is given by Eq. 2, where h_{max} and P_{max} are the maximal depth and load,

respectively; S_u is the unloading contact stiffness; and h_0 is the tip defect. Using the methodology described in [66], the tip defect was evaluated on fused silica (Fig. S3) and found to be around 30 nm. The projected contact area A_c is then given by Eq. 3. The hardness H is finally given by Eq. 4. It is worth noting that within the framework of this paper, we deliberately focused only on hardness measurements and not on computation of the Young's modulus. However, evolution of the Young's modulus with temperature is given in Fig. S4.

$$h_c = 1.2(h_{max} - \frac{P_{max}}{S_u} + h_0) \quad \text{Eq. 2}$$

$$A_c = 24.5 \cdot h_c^2 \quad \text{Eq. 3}$$

$$H = \frac{P_{max}}{A_c} \quad \text{Eq. 4}$$

These equations are still valid for CSM measurement analysis. In this case, the dynamic stiffness S is used instead of the unloading stiffness S_u, and the instantaneous load P and depth h are used instead of the maximal load and depth P_{max} and h_{max}.

3.2 Analysis of creep segment

The creep segment was analyzed using the methodology described by Baral et al. [68]. This methodology is based on the definition of a representative stress σ_r and a representative strain rate $\dot{\epsilon_r}$.

The representative stress σ_r is related to the hardness H by Eq. 5, where γ is the constraint factor as defined by Kermouche et al. [69]. This constraint factor is given by Eq. 6, with $\theta = 70.32°$, the equivalent cone apex semi-angle of the Berkovich tip, $E = 70$ GPa, the Young's modulus of the material, $\xi_1 = 0.66$, $\xi_2 = 0.216$, and $\xi_3 = 0.24$. The representative strain rate is related to the indentation strain rate $\dot{h}/h$ by Eq. 7, where m is the strain-rate sensitivity.

$$\sigma_r = \frac{H}{\gamma} \quad \text{Eq. 5}$$

$$\gamma = \frac{\xi_1 \cdot \cot(\theta) - (1 - \xi_2)H/E}{\xi_3 \cot(\theta)} \quad \text{Eq. 6}$$

$$\dot{\epsilon_r} = 0.44 \cdot \cot(\theta) \cdot \exp\left(\frac{0.2}{m}\right) \dot{h}/h \quad \text{Eq. 7}$$

By analogy with a uniaxial tensile test, the representative stress σ_r can then be related to the representative strain rate $\dot{\epsilon_r}$ by a power-law relation, as expressed in Eq. 8, where α is the strength coefficient. From those equations, it appears that a linear fit of $\ln(\dot{h}/h)$ versus $\ln(\sigma_r)$ gives access to both the strain-rate sensitivity m and the strength coefficient α.

$$\dot{\epsilon_r} = \alpha \sigma_r^{\left(\frac{1}{m}\right)} \quad \text{Eq. 8}$$

4 Results and discussion

HTSI measurements were performed on two ZrCu thin films from the same deposition batch. This method allowed us to independently follow the hardness and strain-rate sensitivity evolutions during an entire thermal cycle. The resulting hardness values, computed from the unloading part of the indentation curve, are given in Fig. 2 for the two samples (identified as ZrCu #1 and ZrCu #2). The hardness evolution is drawn against the testing time (Fig. 2a) as well as against the testing temperature (Fig. 2b). In addition to these results, the strain-rate sensitivity coefficient m was extracted from the creep segment of each indentation test. The results are plotted against the testing time (Fig. 3a) and the testing temperature (Fig. 3b).

It appears from Fig. 2 and 3 that the hardness and strain-rate sensitivity evolution during a thermal cycle can be described in three stages, corresponding to different mechanical responses of the ZrCu coatings. Thus, during the first stage, from room temperature to ~500 K, both the hardness and strain-rate sensitivity are roughly constant. Then, the hardness greatly decreases, whereas the strain-rate sensitivity increases, which consists of the second stage in Fig. 2 and 3. Finally, the hardness starts to increase, whereas the strain-rate sensitivity decreases, which marks the beginning of stage 3. The purpose is now to discuss

each of these stages in regard to the physical changes that occur within the coatings and in regard to the three possible material states for the coatings: metallic glass, supercooled liquid, and crystallized. The results are then compared and balanced with DSC and XRD measurements.

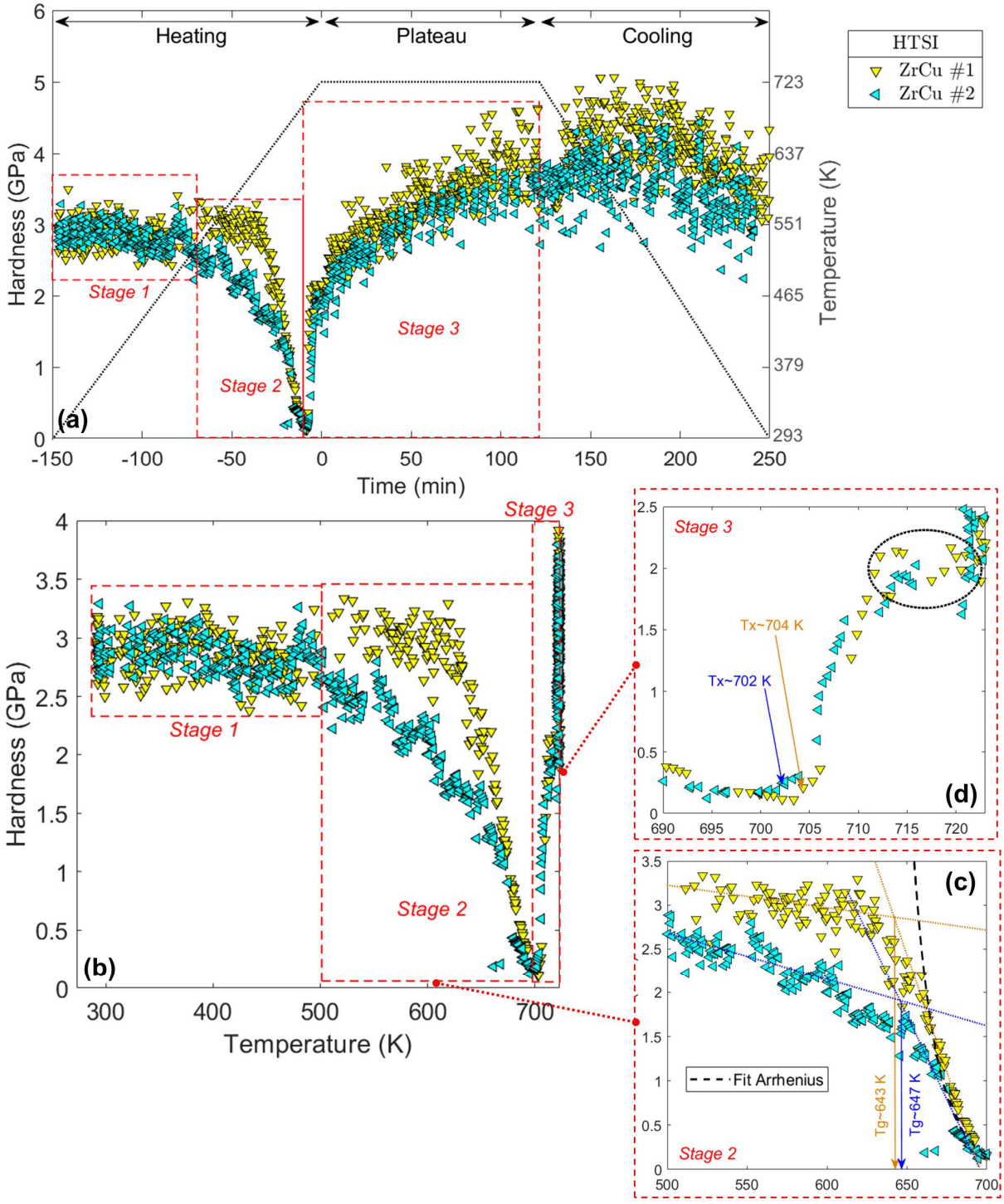

FIG. 2: Hardness evolution of two ZrCu thin films from HTSI measurements during the entire thermal cycle plotted against the testing time (with time = 0 corresponding to the beginning of the 2-h plateau at

723 K) (a) and the testing temperature (heating ramp only) (b). The results reveal three stages corresponding to the initial metallic glass state (stage 1), the metallic glass-to-supercooled liquid region transition (stage 2), and the crystallization step (stage 3). For the clarity of Fig. 2b, the hardness measured during cooling is not plotted; however, the full hardness versus temperature plots are presented in Fig. S5. A highlight of stage 2 and the non-isothermal part of stage 3 are given in (c) and (d), respectively, showing T_g and T_x. In (c), the dotted line corresponds to an Arrhenius fit of the hardness in the supercooled liquid region. In (d), a hardness plateau suggests a break in the crystallization after a first crystallization step during the ramp (dark dotted ellipse).

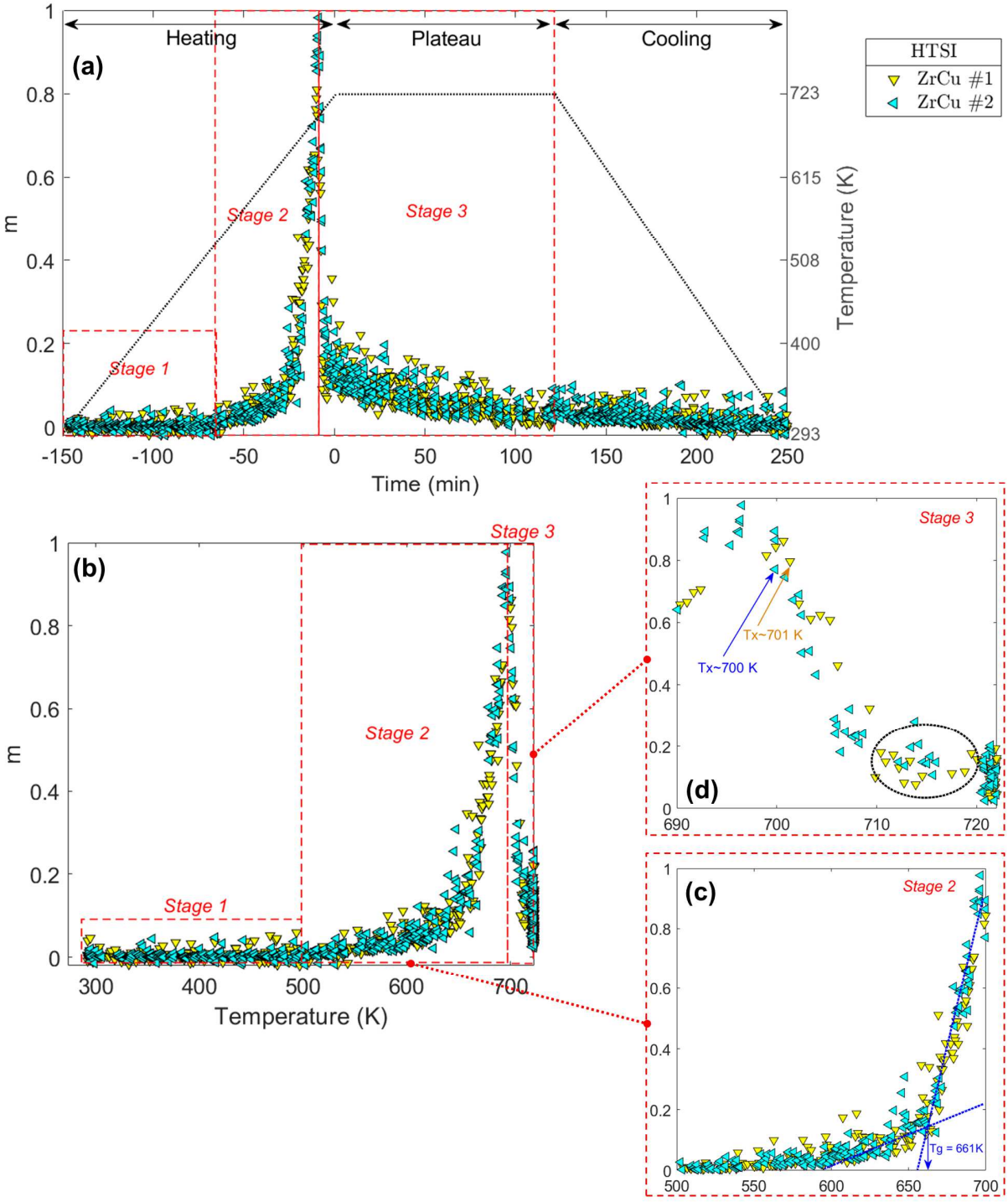

FIG. 3: Strain-rate sensitivity evolution of two ZrCu thin films from HTSI measurements during an entire thermal cycle plotted against testing time (with time = 0 corresponding to the beginning of the 2-h plateau at 723 K) (a) and the testing temperature (heating ramp only) (b). Full strain-rate sensitivity versus temperature plots are presented in Fig. S6. The same stages as those observed on Fig. 2 can be observed here. T_g and T_x can also be determined from (c) and (d).

4.1 Stage 1: Metallic glass state

The purpose of this part is to confirm the initial metallic glass state of the ZrCu coatings and to discuss the mechanical behavior observed in stage 1 of Fig. 2 and 3 in regards to this state.

First, the initial metallic glass state of the ZrCu coatings was confirmed using multiscale techniques. At a global scale, the initial amorphous structure of the films was controlled by XRD (Fig. S7). The maximum of the characteristic hump of amorphous material is centered at 38.6° on the 2θ scale, which is fully consistent with the literature for this composition [26, 42, 70]. At the mesoscopic scale, SEM observations of the coating revealed a homogeneous surface (Fig. S8), with a submicrometric substructure due to columnar growth of the film during the deposition. A cross-section of the film fracture after the substrate cleavage exhibits a vein-like pattern (Fig. S9), which is another characteristic of metallic glass [26, 71-76]. SEM observations also confirm the absence of micrometric precipitates. Finally, examination of the structure at the atomic scale was conducted using TEM observations (Fig. S10). The results confirmed the absence of nanocrystallites and an amorphous atomic distribution of the initial state of ZrCu TFMGs.

The HTSI measurements enable the mechanical properties of the ZrCu coatings from this initial metallic glass state to be followed. Fig. 2 and 3 show that both the hardness and strain-rate sensitivity are first roughly constant from room temperature to roughly 500 K, which corresponds to ~0.76T_g (based on the T_g obtained by DSC at 3 K min^{-1}). This corresponds to the so-called “stage 1”, where no detectable physical changes occur within the sample. The constant hardness of metallic glasses up to roughly 0.7T_g has already been established in the literature [16, 71, 77, 78]. These results confirm that within this stage, the sample remains in a metallic glass state.

Quantitatively, the hardness and strain-rate sensitivity are observed to be approximately 3 GPa and close to zero, respectively: the material is hard, and its flow stress does not depend on the strain-rate sensitivity. The value of hardness is slightly lower than the values in the literature for similar composition at room temperature [41, 70, 79, 80]; however, the computation of the hardness is contact-model dependent, which explains such differences.

4.2 Stage 2: Metallic glass-to-supercooled liquid transition

Above 500 K, the hardness strongly decreases from 3 GPa down to values as low as 0.1 GPa at approximately 700 K (Fig. 2c). At the same time, the strain-rate sensitivity increases up to values close to unity at approximately 690 K (Fig. 3c). This corresponds to stage 2 in Fig. 2 and 3. This strong decrease of the hardness and increase of the strain-rate sensitivity is the signature of a transition that occurs within TFMGs at high temperature. In this stage, the metallic glass starts to behave more like a fluid: the material becomes softer, and its flow stress highly depends on the strain rate. This behavior characterizes the change from a metallic glass to a supercooled liquid that occurs around T_g. The purpose of this part is to fully characterize this transition, as well as the supercooled liquid state, based on the mechanical results.

4.2.1 Identification of the glass transition temperature

The first-level analysis of the hardness and strain-rate sensitivity curves at stage 2 allows us to estimate T_g of the ZrCu coatings. The sharp change in hardness and strain-rate sensitivity between the metallic glass region and the supercooled liquid region (Fig. 2c and Fig. 3c) can be analyzed based on thermomechanical analysis methods [9, 81]. The intersection of the tangents of the curves in the metallic glass region and in the supercooled liquid region gives a reproducible transition temperature of approximately 645 K from the hardness curve, and 661 K from the strain-rate sensitivity curve. It is worth noting that these values are close to the glass transition temperature obtained by DSC measurements, with T_g = 658 K for the 3 K min^{-1} heating ramp (Table 1). These results confirm the clear ability of nanohardness and strain-rate sensitivity measurements during HTSI to be used as "DSC-like" techniques.

It should be noted that the hardness results near T_g were not perfectly reproducible between the two tested samples. Both transition temperatures are the same; however, the decrease in the hardness of ZrCu #2 was much less abrupt than that for ZrCu #1, indicating that the metallic glass-to-supercooled liquid transition was much slower for ZrCu #2 than for ZrCu #1. This result suggests that this transition depends on additional factors, such as local heterogeneities [82]. In this case, HTSI could provide information on the local heterogeneity of samples, given the locale nature of the measurements. However, more analysis would be required to confirm it.

4.2.2 Brittle-to-ductile transition ($T < T_g$)

During heat treatment, BMGs are characterized by a brittle-to-ductile transition that occurs between $0.7T_g$ and $1.1T_g$, according to the literature [8, 16, 53, 71, 77, 78, 83]. This brittle-to-ductile transition is responsible for the hardness loss and the increase in strain-rate sensitivity, which is shown in Fig. 2c and Fig. 3c, respectively, for temperatures from 500 K to 700 K (*i.e.* 0.76 T_g and 1.06 T_g). Thus, the mechanical evolution of these ZrCu TFMGs is similar to the mechanical evolution of metallic glass in bulk state. This was expected, since the thickness of the investigated films (~ 6 µm) is well above the characteristic size of initial shear bands [84].

This brittle-to-ductile transition can also be investigated by a quantitative study of the serrated plastic flow during nanoindentation. Indeed, nanoindentation curves of metallic glasses are characterized by an inhomogeneous plastic flow and the presence of numerous discrete plastic events [51, 83, 85-87], as shown in Fig. 4a. These serrations result from the dynamic of the activation of individual shear bands during deformation [78, 88-91]. As evidence of this shear band dynamic, some emerging shear bands can be observed in post-mortem SEM observations near the indentation imprint, as shown in Fig. 4b. Following the analysis of Schuh and Nieh [51, 78, 86], the contribution of these serrations to the total plastic deformation can be computed as the sum of the total length of each event ($\Delta h_{discrete}$) divided by the final plastic depth ($h_{plastic}$). The results during the heating ramp of the two tested samples are presented in Fig. 4c with respect to the normalized temperature T/T_g (with T_g = 658 K). Bell-shaped curves are obtained.

These bell-shaped curves are evidence of two thermally dependent competing mechanisms [17, 78]: with increasing temperature, the energy barrier to produce shear bands is lowered, leading to an increase in the contribution of the shear bands to the total deformation. However, upon further increasing the temperature, the metallic glass starts to behave like a fluid: the deformation becomes homogeneous, and the contribution of the shear bands to the total deformation decreases. This point corresponds to the brittle-to-ductile transition. According to Fig. 4c, this transition occurs between $0.8T_g$ and $0.9T_g$, which is consistent with the literature [8, 16, 53, 71, 77, 78, 83].

It has also been shown in the literature that these serrations are also strain-rate dependent [16, 51, 78, 83, 86, 87] and vanish for high indentation strain rates. To highlight this effect, the HTSI measurements in Fig. 4c are compared with those obtained for ZrCu TFMGs tested under isothermal conditions with the same nanoindentation testing conditions as well as with a lower and constant nanoindentation strain rate of 0.05 s^{-1} (CSM measurements). It should be noted that the strain rate during high-speed nanoindentation is not constant because of the quarter sinus loading but rapidly decreases toward a roughly constant value close to 2 s^{-1}.

As shown in the literature, Fig. 4c provides evidence that the contribution of the serrations to the total plastic deformation is much lower for the highest strain rate. This strain-rate dependency of the serrations is explained in the literature by the dynamic of the nucleation and propagation of individual or multiple shear bands during deformation. For low strain rate, once a single shear band is initiated, the deformation is slow enough that this individual shear band has enough time to grow and accommodate the deformation. This leads to a visible strain burst in the nanoindentation curve. In contrast, at high strain rate, an individual shear band does not have time to grow and entirely accommodate the deformation. This leads to the nucleation of simultaneous operating multiple shear bands during the deformation, which is responsible for a more homogeneous flow [17, 78, 85]. These explanations have been correlated to post-mortem observations of indentation imprints [91, 92].

Thus, the results from the HTSI tests are perfectly consistent with the literature and especially with the temperature and strain-rate deformation map proposed by Schuh et al. [17, 78]. This shows the ability of HTSI to follow the brittle-to-ductile transition in metallic glass, not only using the hardness and nanoindentation strain-rate sensitivity but also from the study of the serrated plastic flow during loading. In addition, with the high nanoindentation speed of HTSI, numerous tests can be performed during a thermal cycle, allowing real-time monitoring of these events with temperature.

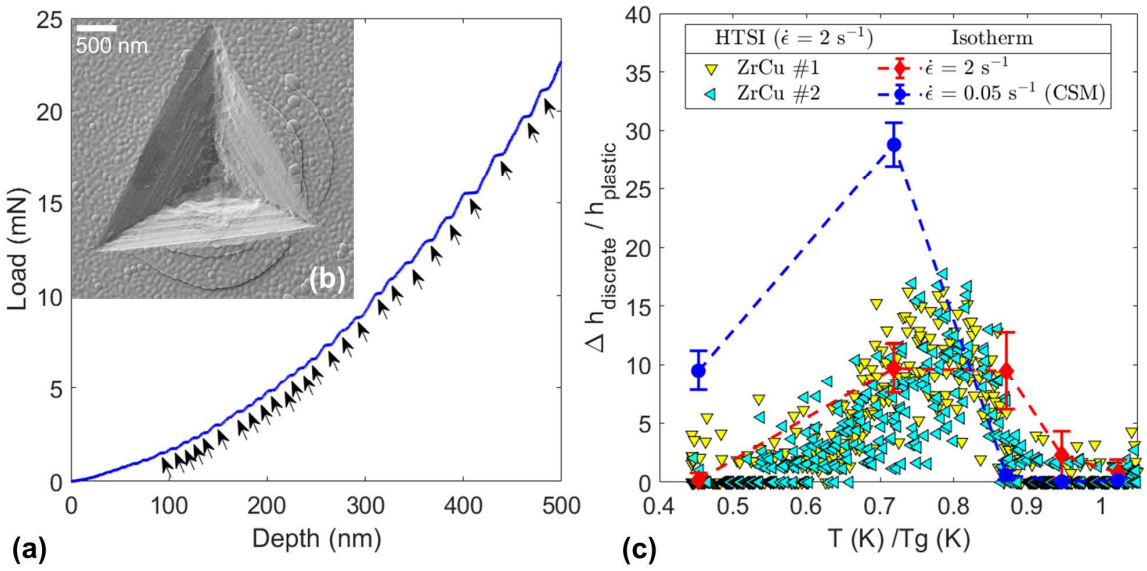

FIG. 4: Example of typical serrated flow during indentation of a metallic glass (CSM mode at 473 K), with several discrete events indicated by black arrows (a) and resulting emerging shear bands on post-mortem SEM images (b). The contribution of these serrations to the total deformation of the ZrCu TFMG indented under different testing conditions (strain rate and temperature) is given in (c). T_g = 658 K.

4.2.3 From HTSI to kinetic… (T_g<T< T_x)

Above T_g, ZrCu coatings are in a supercooled liquid state, which is characterized by fluid-like behavior with low hardness and high strain-rate sensitivity. It is worth noting that in the supercooled-liquid region, the strain-rate sensitivity values suggest that the supercooled liquid behaves first as a non-Newtonian fluid ($m < 1$) and becomes increasingly Newtonian with increasing temperature, with the strain rate sensitivity finally reaching 1 nearly at the end of stage 2.

Going even deeper in the study of this physical state, the Sherby and Armstrong analysis of creep and self-diffusion in metallic crystalline materials [93] can be used to estimate the activation energy responsible for the thin-film deformation at this state. This analysis relates the strain rate to the stress using an Arrhenius law, as given by Eq. 9, where Q_L is the activation energy for lattice self-diffusion, n is the creep stress exponent, R is the gas constant, and B is a material constant. By extending this analysis to amorphous materials, it leads to an Arrhenius dependency of the ratio $\dot{\epsilon}_r/\sigma^n$. One can notice that within these conditions, $n = 1/m$.

$$\dot{\epsilon_r} = Bexp\left(-\frac{Q_L}{RT}\right)\sigma^n \qquad \text{Eq. 9}$$

The activation energy Q_L involved in Eq. 9 corresponds to the energy required for the activation of the mechanism responsible for the accommodation of the plastic deformation during the indentation creep segment. This energy can be obtained by fitting $\ln(\dot{\epsilon_r}/\sigma^n)$ versus the reverse temperature over the supercooled liquid region, *i.e.,* from T_g to T_x. The results for the two tested samples are presented in Fig. 5. Although results appear to be a bit noisy, due to cumulative noise of both hardness and strain rate sensitivity measurements, the expected trend is observed and the resulting activation energy is measured to be approximately 150 ± 30 kJ mol−1, or 1.6 eV +/- 0.3 eV. This result is close to values obtained by Faupel et al. for the activation energy of the diffusion of copper atoms in ZrNi metallic glasses [94]. It also corresponds to the same order of magnitude as the activation energy of relaxation processes linked to the diffusion motion of the smallest constituent atom in metallic glasses [82, 95].

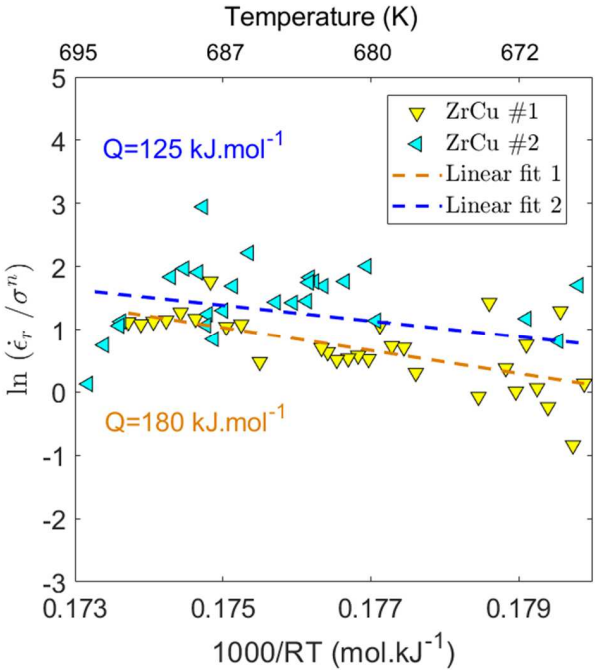

FIG. 5: Determination of the activation energy for creep deformation for the supercooled liquid region of ZrCu TFMGs from the linear fitting of $\ln(\dot{\epsilon_r}/\sigma^n)$ versus $1/RT$.

4.3 Stage 3: Crystallization

The third stage in Fig. 2 and 3 corresponds to the increase in hardness and decrease in strain-rate sensitivity from 703 K to the end of the 723-K plateau. This stage can be divided into two parts depending on the thermal cycle applied: a part from 703 to 723 K, which corresponds to the end of the heating ramp (non-isothermal conditions), and a part that corresponds to the 2-h plateau at 723 K (isothermal conditions).

During the heating from 703 to 713 K, the hardness increases sharply from 0.1 to 2 GPa before remaining constant up to the 2-h plateau at 723 K (Fig. 2d). In parallel, from 697 to 710 K, the strain-rate sensitivity and drastically falls from 1 to 0.1–0.2 before remaining constant up to the 723-K plateau (Fig. 3d). These results are due to crystallization, which occurs within the coatings at this stage. Crystallized material is obviously harder than the supercooled liquid, which causes the sharp increase in hardness. Moreover, because of crystallization, the material no longer behaves like a fluid, and the strain-rate sensitivity falls. The onset of crystallization temperature T_x is measured at approximately 703 K on the hardness curve (Fig. 2d) and at approximately 700 K (Fig. 3d) on the strain-rate sensitivity curve. These results are approximately 20-K higher than the T_x obtained by DSC for the 3 K min^{-1} heating rate condition. This difference can be explained by two factors: first, nanoindentation tests give a mean value of the mechanical properties of the material over a few square micrometers. Thus, they can lead to a lack of sensitivity in the first stage of crystallization, where crystallites are too small to be mechanically assessed. Moreover, the nanoindenter is a local probe, and crystallization may not be detected if the indentation is conducted on a crystallite-free area.

After this first crystallization step, both the hardness and strain-rate sensitivity remain roughly constant during the heating from 713 to 723 K (Fig. 2d and 3d), which suggests that crystallization has stopped. However, soon after the beginning of the 723-K plateau, the hardness increases again from 2 to 4 GPa (Fig. 2a), and the strain-rate sensitivity slowly decreases down to roughly 0.01–0.05 (Fig. 3a); however, both processes occur with much slower kinetics. This finding suggests that crystallization has started again during the plateau.

At the end of the plateau and during the cooling down, both the hardness and strain-rate sensitivity values are roughly constant, which indicates that crystallization has stopped.

Post-mortem XRD (Fig. 6) reveals that the sample was crystallized at roughly 80% after the entire thermal cycle. The obtained phases are the body-centered orthorhombic (bco) $Cu_{10}Zr_7$ and the tetragonal (t) Zr_2Cu; however, surprisingly, there was also evidence of the cubic (c) ZrCu phase. Indeed, both bco-$Cu_{10}Zr_7$ and t-Zr_2Cu are the two thermodynamically stable phases at 723 K; however, the c-ZrCu phase is metastable at temperatures below 988 K and decomposes into bco-$Cu_{10}Zr_7$ and t-Zr_2Cu upon cooling [96]. However, even though bco-$Cu_{10}Zr_7$ and t-Zr_2Cu are the most common phases in the literature for these compositions and temperatures [26, 42], there is some evidence in the literature of the presence of the metastable c-ZrCu phase when a ZrCu metallic glass is rapidly heated and quenched or when it exhibits a slow diffusion rate and high viscosity [97].

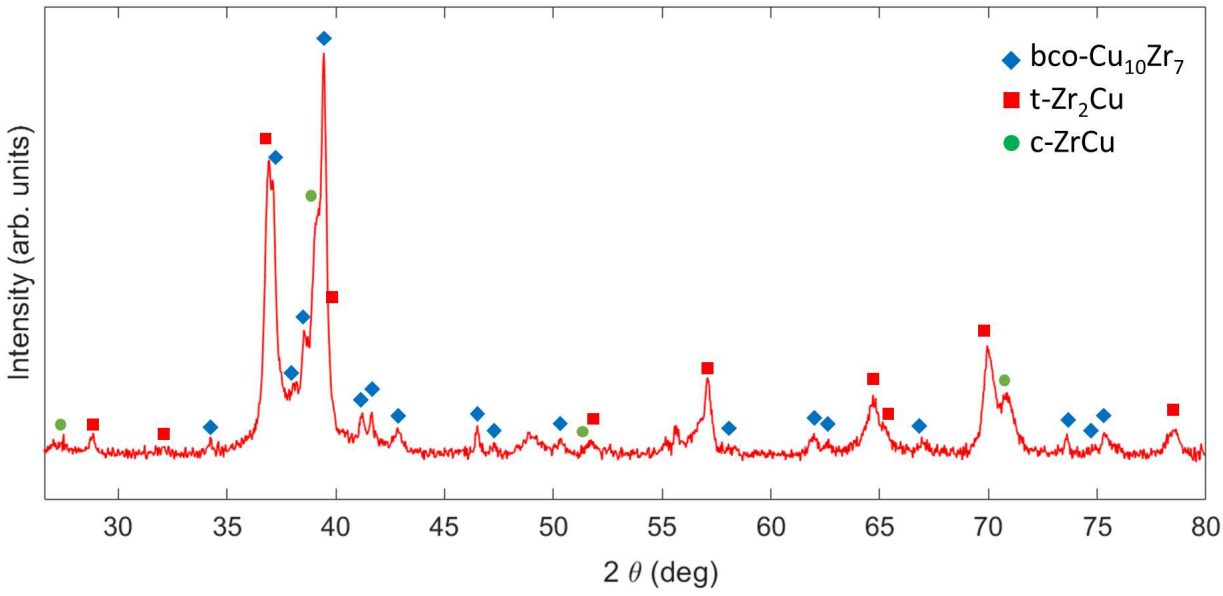

FIG. 6: Post-mortem XRD diffractogram of partially crystallized ZrCu thin films, showing evidence of body-centered orthorhombic $Cu_{10}Zr_7$, tetragonal Zr_2Cu, and cubic ZrCu phases. The crystallization fraction is observed to be approximately 80%.

To better investigate the crystallization kinetics involved during stage 3, the crystallized fraction can be computed from the hardness measurements. Considering an iso-strain assumption during nanoindentation

of ZrCu coatings, the effective hardness of the supercooled liquid + crystallites composite can be described by a mixture law. The crystallized fraction X is then given by Eq. 10, where H is the measured hardness, H_a is the hardness of a theoretically 100% amorphous ZrCu thin film, and H_x is the hardness of a theoretically 100% crystallized ZrCu thin film.

$$X = \frac{H - H_a}{H_x - H_a} \qquad \text{Eq. 10}$$

Both H_a and H_x are supposed to depend on the temperature. In particular, it has been shown that the hardness of the amorphous phase greatly decreases with temperature within the supercooled liquid region. This trend can be simply fitted with an Arrhenius-like law, as shown in Fig. 2c, and used to model H_a during the entire crystallization process.

Moreover, the roughly constant value of the hardness during the cooling down (Fig. 2b) indicates that the hardness of the crystallized phase does not evolve within the investigated range of temperature (from T_x~700 K to 2-h plateau at 723 K). The value of H_x can then be determined by solving Eq. 10 for the 80%-crystallized final ZrCu coatings. The value of H_x has been observed to be approximately 4.5 GPa.

Using Eq. 10 during the entire crystallization process, the crystallized fraction can then be computed from the hardness values. The results during the ramp and plateau of the thermal cycle are presented in Fig. 7. For comparison purpose, the crystallization fractions computed from *in situ* HT-XRD measurements are also shown. The results indicate the remarkable agreement between the techniques. One of the main advantages of HTSI is the large amount of measurements allowed by this technique in a really short time. However, because of the local nature of nanoindentation testing, HTSI fails to assess the early stages of crystallization, in comparison with XRD. Nevertheless, this local nature also gives key-information on the sample heterogeneity, especially after the partial crystallization, where the span of the results suggests a difference of the crystallization fraction of roughly 20 points. Thus, HTSI can be seen as a complementary approach to XRD, which may corresponds to the intermediary scale between mesoscopic and nanoscopic scales.

It is worth noting that the iso-strain assumption leading to Eq. 10 corresponds to an upper limit of the hardness. The literature has shown that this assumption was well verified for soft matrix and hard particle composites with high volume fraction (typically higher than 40%–50%) [98, 99]. In the current case, this condition is rapidly met after the first sharp increase of hardness from 703 to 713 K.

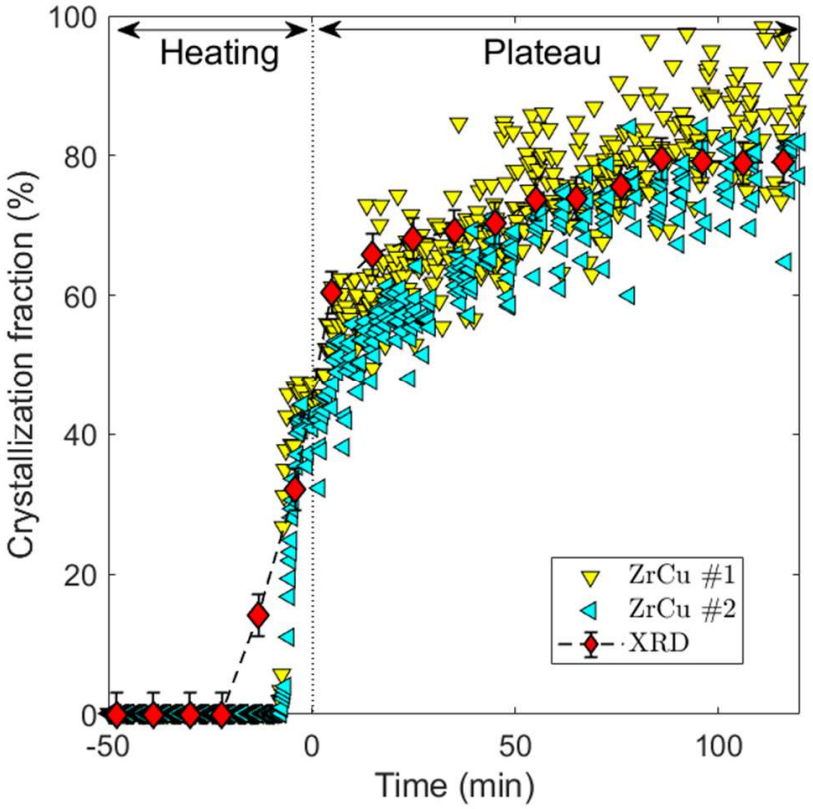

FIG. 7: Crystallization fraction computed from hardness values as well as from HT-XRD measurements plotted against the testing time, where time = 0 corresponds to the beginning of the 2-h plateau at 723 K. The error bar on data points from the XRD measurements corresponds to an estimation of the error made by considering only the XRD peaks from 27° to 47° instead of the entire 2θ range.

In addition, both the HT-XRD and HTSI techniques illustrate the double kinetics of crystallization within ZrCu TFMGs, with a first fast crystallization during the heating ramp, and then a slower crystallization during the 2-h plateau. This slowest crystallization that occurs during the 2-h plateau could be explained by the competition between the nucleation and growth of several intermetallics.

Indeed, Fig. 8 shows the *in-situ* HT-XRD diffractograms during a similar thermal cycle. These results indicate that at the end of the heating ramp and at the beginning of the 2-h plateau, the three intermetallics bco-Zr_7Cu_{10}, t-Zr_2Cu, and c-ZrCu crystallized. It should be noted that some oxidation also occurred at high temperature, with the formation of tetragonal (t) ZrO_2 and monoclinic (m) ZrO_2, as also shown in the literature [26]. However, after a first crystallization of the bct-Zr_7Cu_{10}, t-Zr_2Cu, and c-ZrCu phases, the peaks corresponding to the c-ZrCu phase deeply decrease during the 723-K plateau, whereas the peaks corresponding to the bct-Zr_7Cu_{10} and t-Zr_2Cu phases continued to increase. This result indicates that the metastable c-ZrCu phase disappears and transforms into the two thermodynamically stable phases. In parallel, the amorphous hump still decreases, which indicates that the crystallization process still occurs. Thus, both crystallization and phase transformation are involved during the 723 K plateau, which could explain the slower crystallization kinetics involved at this step. Such phase competition could also be an explanation for the short pause in the crystallization process at the end of the heating ramp.

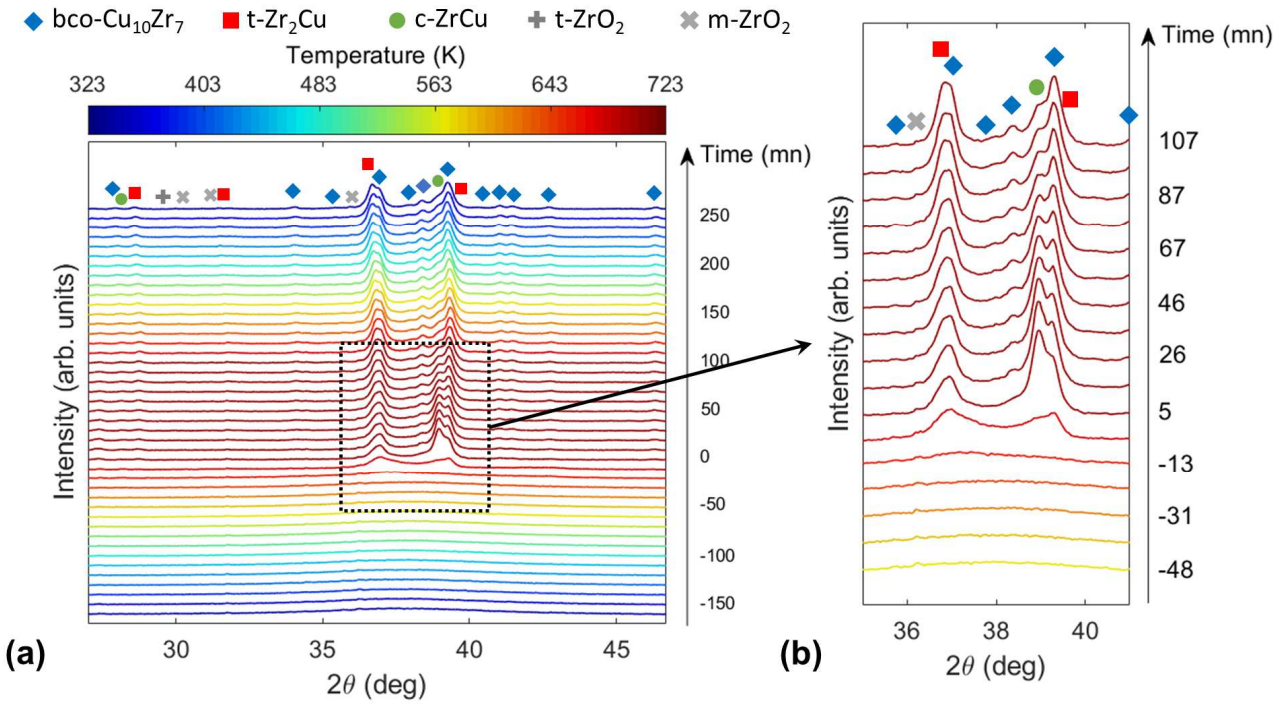

FIG. 8: HT-XRD diffractograms of ZrCu coatings measured during an entire thermal cycle (a) with the color scale corresponding to the temperature. The diffractograms are shifted along the y-axis according to the testing time, with time = 0 for the beginning of the 2-h plateau at 723 K. A zoomed-in version of the diffractograms during the

crystallization process (end of the heating ramp and plateau) is given in (b).

5 Conclusion

This work reports for the first time the use of a new technique, high-temperature scanning indentation (HTSI), to measure in real-time and at the local scale the physical changes involved during the heat treatment of a model TFMG. This high-speed nanoindentation technique overcomes the limitation of high temperature nanoindentation due to thermal drift, and allows real-time nanohardness and creep measurements during non-isothermal cycles. The thermal evolution of hardness and strain-rate sensitivity are interpreted as a "DSC-like" technique to determine *in-situ* physical changes occurring within the material. This establishes HTSI as the first stand-alone technique, able to follow the entire mechanical evolution in temperature of small-scale materials in only a few hours. In particular, hundreds of data point can be obtained in only one batch, making HTSI a competitive technique compared to tensile or compression tests in temperature.

Thus, based on the study of ZrCu TFMG, HTSI allowed the three physical states taken by the material during heat treatment to be clearly identified: metallic glass, supercooled liquid, and crystallized. In particular, the mechanical response of the ZrCu thin film has been assessed *in-situ* during the entire supercooled liquid stage, leading to key information about the kinetics.

The transition from metallic glass to supercooled liquid and the crystallization were successively detected by HTSI, leading to identification of the glass transition temperature T_g and crystallization temperature T_x, with good consistency with the DSC measurements. Moreover, the brittle-to-ductile transition has also been precisely characterized, with remarkable agreement with the literature [17, 78]. Similarly, the crystallization fraction deduced from HTSI was found to be very consistent with that obtained by HT-XRD. This has shown the excellent match obtained for behaviors recorded with a local probe or with an averaged volume at the meso-scale.

Finally, the robustness of HTSI to study thermally activated mechanisms in thin films has been demonstrated. Moreover, because of the local nature of the measurements, HTSI opens up the prospect of investigating such mechanisms at an even lower scale – by diminishing either the indentation size or the film thickness – to put in light new small-scale mechanisms. In addition, thanks to the fast indentation rate during HTSI, which leads to complete *in-situ* characterization in merely a few hours, it also offers the prospect for the fast characterization of tailored materials with dedicated properties.

Data availability statement

The data that support the findings of this study are available from the corresponding author upon reasonable request.

Declaration of competing interest

The authors declare that they have no known competing financial interests or personal relationships that could have appeared to influence the work reported in this paper.

Acknowledgements

This work was supported by the MEGALIT and RATES ANR projects (grant ANR-18-CE08-0018 and ANR-20-CE08-0022) of the French Agence Nationale de la Recherche, by the EUR MANUTECH-Sleight funding, and by the FORMEL project from the Region Auvergne-Rhones-Alpes. The Centre de Compétences Daum of the Institut Jean Lamour is acknowledged for its technical support. Authors also thank the CLYM platform for providing access to the FEI-TITAN eTEM.

This collaborative work was initiated with the help of Florence Garrelie (Laboratoire Hubert Curien, France). Authors would like also to thank Paul Baral (IMMC UCLouvain, Belgium) and Warren Oliver (KLA Nanomechanics Inc., USA) for their constructive discussion on experimental procedures, and for their help on the method development. In addition, authors thank Jean-Marc Pelletier (INSA de Lyon, France) for is stimulating discussion, and careful proofreading of the paper.

References

[1] W. Klement, R.H. Willens, P. Duwez, Non-crystalline Structure in Solidified Gold–Silicon Alloys, Nature. 187 (1960) 869–870. https://doi.org/10.1038/187869b0.

[2] H.S. Chen, D. Turnbull, Evidence of a Glass–Liquid Transition in a Gold–Germanium–Silicon Alloy, J. Chem. Phys. 48 (1968) 2560–2571. https://doi.org/10.1063/1.1669483.

[3] W.L. Johnson, Bulk amorphous metal—An emerging engineering material, JOM. 54 (2002) 40–43. https://doi.org/10.1007/BF02822619.

[4] M.F. Ashby, A.L. Greer, Metallic glasses as structural materials, Scripta Materialia. 54 (2006) 321–326. https://doi.org/10.1016/j.scriptamat.2005.09.051.

[5] W.H. Wang, Bulk Metallic Glasses with Functional Physical Properties, Advanced Materials. 21 (2009) 4524–4544. https://doi.org/10.1002/adma.200901053.

[6] J. Schroers, Processing of Bulk Metallic Glass, Adv. Mater. 22 (2010) 1566–1597. https://doi.org/10.1002/adma.200902776.

[7] J.J. Kruzic, Bulk Metallic Glasses as Structural Materials: A Review: Bulk Metallic Glasses as Structural Materials: A Review, Adv. Eng. Mater. 18 (2016) 1308–1331. https://doi.org/10.1002/adem.201600066.

[8] J.-M. Pelletier, J. Qiao, Metallic Glasses, in: J.D. Musgraves, J. Hu, L. Calvez (Eds.), Springer Handbook of Glass, Springer International Publishing, Cham, 2019: pp. 617–643. https://doi.org/10.1007/978-3-319-93728-1_18.

[9] T.W. Tang, Y.C. Chang, J.C. Huang, Q. Gao, J.S.C. Jang, C.Y.A. Tsao, On thermomechanical properties of Au–Ag–Pd–Cu–Si bulk metallic glass, Materials Chemistry and Physics. 116 (2009) 569–572. https://doi.org/10.1016/j.matchemphys.2009.04.032.

[10] A. Inoue, A. Takeuchi, Recent development and application products of bulk glassy alloys, Acta Materialia. 59 (2011) 2243–2267. https://doi.org/10.1016/j.actamat.2010.11.027.

[11] P.H. Tsai, Y.Z. Lin, J.B. Li, S.R. Jian, J.S.C. Jang, C. Li, J.P. Chu, J.C. Huang, Sharpness improvement of surgical blade by means of ZrCuAlAgSi metallic glass and metallic glass thin film coating, Intermetallics. 31 (2012) 127–131. https://doi.org/10.1016/j.intermet.2012.06.014.

[12] S. Li, Q. Wei, Q. Li, B. Jiang, Y. Chen, Y. Sun, Development of Fe-based bulk metallic glasses as potential biomaterials, Materials Science and Engineering: C. 52 (2015) 235–241. https://doi.org/10.1016/j.msec.2015.03.041

[13] M.S. Dambatta, S. Izman, B. Yahaya, J.Y. Lim, D. Kurniawan, Mg-based bulk metallic glasses for biodegradable implant materials: A review on glass forming ability, mechanical properties, and biocompatibility, Journal of Non-Crystalline Solids. 426 (2015) 110–115. https://doi.org/10.1016/j.jnoncrysol.2015.07.018.

[14] H.F. Li, Y.F. Zheng, Recent advances in bulk metallic glasses for biomedical applications, Acta Biomater. 36 (2016) 1–20. https://doi.org/10.1016/j.actbio.2016.03.047.

[15] S. Comby-Dassonneville, T. Venot, A. Borroto, E. Longin, C. der Loughian, B. ter Ovanessian, M.-A. Leroy, J.-F. Pierson, P. Steyer, ZrCuAg Thin-Film Metallic Glasses: Toward Biostatic Durable Advanced Surfaces, ACS Appl. Mater. Interfaces. (2021). https://doi.org/10.1021/acsami.1c01127.

[16] T. Hufnagel, Preface to the viewpoint set on mechanical behavior of metallic glasses, Scripta Materialia. 54 (2006) 317–319. https://doi.org/10.1016/j.scriptamat.2005.10.004.

[17] C.A. Schuh, T.C. Hufnagel, U. Ramamurty, Mechanical behavior of amorphous alloys, Acta Materialia. 55 (2007) 4067–4109. https://doi.org/10.1016/j.actamat.2007.01.052.

[18] A.L. Greer, Metallic glasses…on the threshold, Materials Today. 12 (2009) 14–22. https://doi.org/10.1016/S1369-7021(09)70037-9.

[19] C. Suryanarayana, Mechanical behavior of emerging materials, Materials Today. 15 (2012) 486–498. https://doi.org/10.1016/S1369-7021(12)70218-3.

[20] D.V. Louzguine, H. Kato, A. Inoue, High-strength Cu-based crystal-glassy composite with enhanced ductility, Appl. Phys. Lett. 84 (2004) 1088–1089. https://doi.org/10.1063/1.1647278.

[21] J. Das, M.B. Tang, K.B. Kim, R. Theissmann, F. Baier, W.H. Wang, J. Eckert, "Work-Hardenable" Ductile Bulk Metallic Glass, Phys. Rev. Lett. 94 (2005) 205501. https://doi.org/10.1103/PhysRevLett.94.205501.

[22] S. Cardinal, J.M. Pelletier, G.Q. Xie, F. Mercier, F. Dalmas, Enhanced compressive plasticity in a Cu-Zr-Al – Based metallic glass composite, Journal of Alloys and Compounds. 782 (2019) 59–68. https://doi.org/10.1016/j.jallcom.2018.11.300.

[23] E. Ma, J. Ding, Tailoring structural inhomogeneities in metallic glasses to enable tensile ductility at room temperature, Materials Today. 19 (2016) 568–579. https://doi.org/10.1016/j.mattod.2016.04.001.

[24] Y. Liu, J. Liu, S. Sohn, Y. Li, J.J. Cha, J. Schroers, Metallic glass nanostructures of tunable shape and composition, Nature Communications. 6 (2015) 7043. https://doi.org/10.1038/ncomms8043.

[25] J.P. Chu, J.S.C. Jang, J.C. Huang, H.S. Chou, Y. Yang, J.C. Ye, Y.C. Wang, J.W. Lee, F.X. Liu, P.K. Liaw, Y.C. Chen, C.M. Lee, C.L. Li, C. Rullyani, Thin film metallic glasses: Unique properties and potential applications, Thin Solid Films. 520 (2012) 5097–5122. https://doi.org/10.1016/j.tsf.2012.03.092.

[26] M. Apreutesei, P. Steyer, A. Billard, L. Joly-Pottuz, C. Esnouf, Zr–Cu thin film metallic glasses: An assessment of the thermal stability and phases' transformation mechanisms, Journal of Alloys and Compounds. 619 (2015) 284–292. https://doi.org/10.1016/j.jallcom.2014.08.253.

[27] S.I. Bulychev, V.P. Alekhin, M.H. Shorshorov, A.P. Ternovskii, G.D. Shnyrev, Determining Young's modulus from the indentor penetration diagram, Ind. Lab. 41 (1975) 1409–1412.

[28] J.B. Pethica, R. Hutchings, W.C. Oliver, Composition and hardness profiles in ion implanted metals, Nuclear Instruments and Methods in Physics Research. 209–210 (1983) 995–1000. https://doi.org/10.1016/0167-5087(83)90911-0.

[29] J.L. Loubet, J.M. Georges, O. Marchesini, G. Meille, Vickers Indentation Curves of Magnesium Oxide (MgO), Journal of Tribology. 106 (1984) 43–48. https://doi.org/10.1115/1.3260865.

[30] J.L. Loubet, J.M. Georges, G. Meille, Vickers Indentation Curves of Elastoplastic Materials, Microindentation Techniques in Materials Science and Engineering. (1985). https://doi.org/10.1520/STP32952S.

[31] M.F. Doerner, W.D. Nix, A method for interpreting the data from depth-sensing indentation instruments, Journal of Materials Research. 1 (1986) 601–609. https://doi.org/10.1557/JMR.1986.0601.

[32] W.C. Oliver, G.M. Pharr, An improved technique for determining hardness and elastic modulus using load and displacement sensing indentation experiments, Journal of Materials Research. 7 (1992) 1564–1583. https://doi.org/10.1557/JMR.1992.1564.

[33] J.L. Loubet, M. Bauer, A. Tonck, S. Bec, B. Gauthier-Manuel, Nanoindentation with a Surface Force Apparatus, in: M. Nastasi, D.M. Parkin, H. Gleiter (Eds.), Mechanical Properties and Deformation Behavior of Materials Having Ultra-Fine Microstructures, Springer Netherlands, Dordrecht, 1993: pp. 429–447. https://doi.org/10.1007/978-94-011-1765-4_28.

[34] X. Li, B. Bhushan, A review of nanoindentation continuous stiffness measurement technique and its applications, Materials Characterization. 48 (2002) 11–36. https://doi.org/10.1016/S1044-5803(02)00192-4.

[35] W.C. Oliver, G.M. Pharr, Measurement of hardness and elastic modulus by instrumented indentation: Advances in understanding and refinements to methodology, Journal of Materials Research. 19 (2004) 3–20. https://doi.org/10.1557/jmr.2004.19.1.3.

[36] Y.-T. Cheng, C.-M. Cheng, Scaling, dimensional analysis, and indentation measurements, Materials Science and Engineering: R: Reports. 44 (2004) 91–149. https://doi.org/10.1016/j.mser.2004.05.001.

[37] A.C. Fischer-Cripps, Nanoindentation, 3rd ed., Springer-Verlag, New York, 2011. https://doi.org/10.1007/978-1-4419-9872-9.

[38] F. Zeng, Y. Gao, L. Li, D.M. Li, F. Pan, Elastic modulus and hardness of Cu–Ta amorphous films, Journal of Alloys and Compounds. 389 (2005) 75–79. https://doi.org/10.1016/j.jallcom.2004.06.077.

[39] J.-J. Pang, M.-J. Tan, K.M. Liew, C. Shearwood, Nanoindentation study of size effect and loading rate effect on mechanical properties of a thin film metallic glass Cu49.3Zr50.7, Physica B: Condensed Matter. 407 (2012) 340–346. https://doi.org/10.1016/j.physb.2011.10.050.

[40] C.-Y. Chuang, J.-W. Lee, C.-L. Li, J.P. Chu, Mechanical properties study of a magnetron-sputtered Zr-based thin film metallic glass, Surface and Coatings Technology. 215 (2013) 312–321. https://doi.org/10.1016/j.surfcoat.2012.04.101.

[41] M. Apreutesei, P. Steyer, L. Joly-Pottuz, A. Billard, J. Qiao, S. Cardinal, F. Sanchette, J.M. Pelletier, C. Esnouf, Microstructural, thermal and mechanical behavior of co-sputtered binary Zr–Cu thin film metallic glasses, Thin Solid Films. 561 (2014) 53–59. https://doi.org/10.1016/j.tsf.2013.05.177.

[42] P. Zeman, M. Zítek, Š. Zuzjaková, R. Čerstvý, Amorphous Zr-Cu thin-film alloys with metallic glass behavior, Journal of Alloys and Compounds. 696 (2017) 1298–1306. https://doi.org/10.1016/j.jallcom.2016.12.098.

[43] S. Korkmaz, İ.A. Kariper, Glass formation, production and superior properties of Zr-based thin film metallic glasses (TFMGs): A status review, Journal of Non-Crystalline Solids. 527 (2020) 119753. https://doi.org/10.1016/j.jnoncrysol.2019.119753.

[44] H.-B. Yu, W.-H. Wang, K. Samwer, The β relaxation in metallic glasses: an overview, Materials Today. 16 (2013) 183–191. https://doi.org/10.1016/j.mattod.2013.05.002.

[45] J.C. Qiao, J.M. Pelletier, Dynamic Mechanical Relaxation in Bulk Metallic Glasses: A Review, Journal of Materials Science & Technology. 30 (2014) 523–545. https://doi.org/10.1016/j.jmst.2014.04.018.

[46] W.H. Wang, C. Dong, C.H. Shek, Bulk metallic glasses, Materials Science and Engineering: R: Reports. 44 (2004) 45–89. https://doi.org/10.1016/j.mser.2004.03.001.

[47] T. Yamasaki, S. Maeda, Y. Yokoyama, D. Okai, T. Fukami, H.M. Kimura, A. Inoue, Viscosity Measurements of Zr55Cu30Al10Ni5 and Pd40Cu30Ni10P20 Supercooled Liquid Alloys by Using a Penetration Viscometer, Materials Transactions. 46 (2005) 2746–2750. https://doi.org/10.2320/matertrans.46.2746.

[48] J.C. Qiao, S. Cardinal, J.M. Pelletier, H. Kato, Insight on the process ability of bulk metallic glasses by thermo-mechanical analysis and dynamic mechanical analysis, Journal of Alloys and Compounds. 628 (2015) 357–363. https://doi.org/10.1016/j.jallcom.2014.12.166.

[49] H. Kato, Y. Kawamura, A. Inoue, H.S. Chen, Newtonian to non-Newtonian master flow curves of a bulk glass alloy Pd40Ni10Cu30P20, Appl. Phys. Lett. 73 (1998) 3665–3667. https://doi.org/10.1063/1.122856.

[50] Y. Kawamura, T. Shibata, A. Inoue, T. Masumoto, Stress Overshoot in Stress-Strain Curves of Zr65Al10Ni10Cu15Metallic Glass, Materials Transactions, JIM. 40 (1999) 335–342. https://doi.org/10.2320/matertrans1989.40.335.

[51] T.G. Nieh, C. Schuh, J. Wadsworth, Y. Li, Strain rate-dependent deformation in bulk metallic glasses, Intermetallics. 10 (2002) 1177–1182. https://doi.org/10.1016/S0966-9795(02)00146-2.

[52] C. Gauthier, J.-M. Pelletier, Q. Wang, J.J. Blandin, Viscoelastic and viscoplastic properties of bulk metallic glasses: Comparison with oxide glasses and amorphous polymers, Journal of Non-Crystalline Solids. 345–346 (2004) 469–472. https://doi.org/10.1016/j.jnoncrysol.2004.08.067.

[53] M.M. Trexler, N.N. Thadhani, Mechanical properties of bulk metallic glasses, Progress in Materials Science. 55 (2010) 759–839. https://doi.org/10.1016/j.pmatsci.2010.04.002.

[54] J.S.K.-L. Gibson, S. Schröders, C. Zehnder, S. Korte-Kerzel, On extracting mechanical properties from nanoindentation at temperatures up to 1000 °C, Extreme Mechanics Letters. 17 (2017) 43–49. https://doi.org/10.1016/j.eml.2017.09.007.

[55] B. Beake, A. Harris, J. Moghal, D. Armstrong, Temperature dependence of indentation size effects, pile-up and strain rate sensitivity in polycrystalline tungsten from 25-950 C, Nanomechanical Testing in Materials Research and Development VI. (2017). https://dc.engconfintl.org/nanomechtest_vi/72.

[56] B.D. Beake, A.J. Harris, Nanomechanics to 1000 °C for high temperature mechanical properties of bulk materials and hard coatings, Vacuum. 159 (2019) 17–28. https://doi.org/10.1016/j.vacuum.2018.10.011.

[57] C. Minnert, W.C. Oliver, K. Durst, New ultra-high temperature nanoindentation system for operating at up to 1100 °C, Materials & Design. 192 (2020) 108727. https://doi.org/10.1016/j.matdes.2020.108727.

[58] P. Baral, M. Laurent-Brocq, G. Guillonneau, J.-M. Bergheau, J.-L. Loubet, G. Kermouche, In situ characterization of AA1050 recrystallization kinetics using high temperature nanoindentation testing, Materials & Design. 152 (2018) 22–29. https://doi.org/10.1016/j.matdes.2018.04.053.

[59] C. Minnert, H. ur Rehman, K. Durst, Thermally activated dislocation mechanism in Mo studied by indentation, compression and impact testing, Journal of Materials Research. (2021). https://doi.org/10.1557/s43578-021-00126-4.

[60] G. Tiphéne, P. Baral, S. Comby-Dassonneville, G. Guillonneau, G. Kermouche, J.-M. Bergheau, W. Oliver, J.-L. Loubet, High-Temperature Scanning Indentation: A new method to investigate in situ metallurgical evolution along temperature ramps, Journal of Materials Research. (2021). https://doi.org/10.1557/s43578-021-00107-7.

[61] R. Saha, W.D. Nix, Effects of the substrate on the determination of thin film mechanical properties by nanoindentation, Acta Materialia. 50 (2002) 23–38. https://doi.org/10.1016/S1359-6454(01)00328-7.

[62] N. Tayebi, A.A. Polycarpou, T.F. Conry, Effects of substrate on determination of hardness of thin films by nanoscratch and nanoindentation techniques, Journal of Materials Research. 19 (2004) 1791–1802. https://doi.org/10.1557/JMR.2004.0233.

[63] J.R. Jinschek, Advances in the environmental transmission electron microscope (ETEM) for nanoscale in situ studies of gas–solid interactions, Chem. Commun. 50 (2014) 2696–2706. https://doi.org/10.1039/C3CC49092K.

[64] P. Wesseling, B.C. Ko, J.J. Lewandowski, Quantitative evaluation of α-Al nano-particles in amorphous Al87Ni7Gd6—comparison of XRD, DSC, and TEM, Scripta Materialia. 48 (2003) 1537–1541. https://doi.org/10.1016/S1359-6462(03)00127-1.

[65] S. Gravier, P. Donnadieu, S. Lay, B. Doisneau, F. Bley, L. Salvo, J.J. Blandin, Evaluation of the crystal volume fraction in a partially nanocrystallized bulk metallic glass, Journal of Alloys and Compounds. 504 (2010) S226–S229. https://doi.org/10.1016/j.jallcom.2010.05.008.

[66] G. Hochstetter, A. Jimenez, J.L. Loubet, Strain-rate effects on hardness of glassy polymers in the nanoscale range. Comparison between quasi-static and continuous stiffness measurements, Journal of Macromolecular Science, Part B. 38 (1999) 681–692. https://doi.org/10.1080/00222349908248131.

[67] S. Bec, A. Tonck, J.-M. Georges, E. Georges, J.-L. Loubet, Improvements in the indentation method with a surface force apparatus, Philosophical Magazine A. 74 (1996) 1061–1072. https://doi.org/10.1080/01418619608239707.

[68] P. Baral, G. Kermouche, G. Guillonneau, G. Tiphene, J.-M. Bergheau, W.C. Oliver, J.-L. Loubet, Indentation creep vs. indentation relaxation: A matter of strain rate definition?, Materials Science and Engineering: A. 781 (2020) 139246. https://doi.org/10.1016/j.msea.2020.139246.

[69] G. Kermouche, J.L. Loubet, J.M. Bergheau, Extraction of stress–strain curves of elastic–viscoplastic solids using conical/pyramidal indentation testing with application to polymers, Mechanics of Materials. 40 (2008) 271–283. https://doi.org/10.1016/j.mechmat.2007.08.003.

[70] P. Coddet, F. Sanchette, J.C. Rousset, O. Rapaud, C. Coddet, On the elastic modulus and hardness of co-sputtered Zr–Cu–(N) thin metal glass films, Surface and Coatings Technology. 206 (2012) 3567–3571. https://doi.org/10.1016/j.surfcoat.2012.02.036.

[71] C.A. Pampillo, Flow and fracture in amorphous alloys, Journal of Materials Science. 10 (1975) 1194–1227. https://doi.org/10.1007/BF00541403.

[72] F. Spaepen, A microscopic mechanism for steady state inhomogeneous flow in metallic glasses, Acta Metallurgica. 25 (1977) 407–415. https://doi.org/10.1016/0001-6160(77)90232-2.

[73] V.Z. Bengus, E.D. Tabachnikova, J. Miškuf, K. Csach, V. OcelíK, W.L. Johnson, V.V. Molokanov, New features of the low temperature ductile shear failure observed in bulk amorphous alloys, Journal of Materials Science. 35 (2000) 4449–4457. https://doi.org/10.1023/A:1004881612750.

[74] Z.F. Zhang, J. Eckert, L. Schultz, Difference in compressive and tensile fracture mechanisms of Zr59Cu20Al10Ni8Ti3 bulk metallic glass, Acta Materialia. 51 (2003) 1167–1179. https://doi.org/10.1016/S1359-6454(02)00521-9.

[75] F.H. Dalla Torre, A. Dubach, J. Schällibaum, J.F. Löffler, Shear striations and deformation kinetics in highly deformed Zr-based bulk metallic glasses, Acta Materialia. 56 (2008) 4635–4646. https://doi.org/10.1016/j.actamat.2008.05.021.

[76] M. Ghidelli, A. Volland, J.-J. Blandin, T. Pardoen, J.-P. Raskin, F. Mompiou, P. Djemia, S. Gravier, Exploring the mechanical size effects in Zr65Ni35 thin film metallic glasses, Journal of Alloys and Compounds. 615 (2014) S90–S92. https://doi.org/10.1016/j.jallcom.2013.11.154.

[77] G. Abrosimova, A. Aronin, D. Matveev, I. Zverkova, V. Molokanov, S. Pan, A. Slipenyuk, The structure and mechanical properties of bulk Zr50Ti16.5Cu15Ni18.5 metallic glasses, Journal of Materials Science. 36 (2001) 3933–3939. https://doi.org/10.1023/A:1017918121205.

[78] C.A. Schuh, A.C. Lund, T.G. Nieh, New regime of homogeneous flow in the deformation map of metallic glasses: elevated temperature nanoindentation experiments and mechanistic modeling, Acta Materialia. 52 (2004) 5879–5891. https://doi.org/10.1016/j.actamat.2004.09.005.

[79] K.-W. Park, J. Jang, M. Wakeda, Y. Shibutani, J.-C. Lee, Atomic packing density and its influence on the properties of Cu–Zr amorphous alloys, Scripta Materialia. 57 (2007) 805–808. https://doi.org/10.1016/j.scriptamat.2007.07.019.

[80] Z.T. Wang, K.Y. Zeng, Y. Li, The correlation between glass formation and hardness of the amorphous phase, Scripta Materialia. 65 (2011) 747–750. https://doi.org/10.1016/j.scriptamat.2011.06.043.

[81] L. Yang, J.L. Thomason, The thermal behaviour of glass fibre investigated by thermomechanical analysis, J Mater Sci. 48 (2013) 5768–5775. https://doi.org/10.1007/s10853-013-7369-7.

[82] J.C. Qiao, Q. Wang, J.M. Pelletier, H. Kato, R. Casalini, D. Crespo, E. Pineda, Y. Yao, Y. Yang, Structural heterogeneities and mechanical behavior of amorphous alloys, Progress in Materials Science. 104 (2019) 250–329. https://doi.org/10.1016/j.pmatsci.2019.04.005.

[83] C.A. Schuh, Nanoindentation studies of materials, Materials Today. 9 (2006) 32–40. https://doi.org/10.1016/S1369-7021(06)71495-X.

[84] O. Glushko, M. Mühlbacher, C. Gammer, M.J. Cordill, C. Mitterer, J. Eckert, Exceptional fracture resistance of ultrathin metallic glass films due to an intrinsic size effect, Sci Rep. 9 (2019) 8281. https://doi.org/10.1038/s41598-019-44384-z.

[85] C.A. Schuh, T.G. Nieh, A nanoindentation study of serrated flow in bulk metallic glasses, Acta Materialia. 51 (2003) 87–99. https://doi.org/10.1016/S1359-6454(02)00303-8.

[86] C.A. Schuh, T.G. Nieh, A survey of instrumented indentation studies on metallic glasses, Journal of Materials Research. 19 (2004) 46–57. https://doi.org/10.1557/jmr.2004.19.1.46.

[87] T. Burgess, M. Ferry, Nanoindentation of metallic glasses, Materials Today. 12 (2009) 24–32. https://doi.org/10.1016/S1369-7021(09)70039-2.

[88] W.J. Wright, R. Saha, W.D. Nix, Deformation Mechanisms of the Zr40Ti14Ni10Cu12Be24 Bulk Metallic Glass, MATERIALS TRANSACTIONS. 42 (2001) 642–649. https://doi.org/10.2320/matertrans.42.642.

[89] Y.I. Golovin, V.I. Ivolgin, V.A. Khonik, K. Kitagawa, A.I. Tyurin, Serrated plastic flow during nanoindentation of a bulk metallic glass, Scripta Materialia. 45 (2001) 947–952. https://doi.org/10.1016/S1359-6462(01)01116-2.

[90] A.L. Greer, A. Castellero, S.V. Madge, I.T. Walker, J.R. Wilde, Nanoindentation studies of shear banding in fully amorphous and partially devitrified metallic alloys, Materials Science and Engineering: A. 375–377 (2004) 1182–1185. https://doi.org/10.1016/j.msea.2003.10.032.

[91] W.H. Jiang, M. Atzmon, Rate dependence of serrated flow in a metallic glass, Journal of Materials Research. 18 (2003) 755–757. https://doi.org/10.1557/JMR.2003.0103.

[92] D. Xing, T. Zhang, W. Li, B. Wei, The characterization of plastic flow in three different bulk metallic glass systems, Journal of Alloys and Compounds. 433 (2007) 318–323. https://doi.org/10.1016/j.jallcom.2006.06.077.

[93] O.D. Sherby, P.E. Armstrong, Prediction of activation energies for creep and self-diffusion from hot hardness data, Metall Mater Trans B. 2 (1971) 3479–3484. https://doi.org/10.1007/BF02811630.

[94] F. Faupel, W. Frank, Diffusion in metallic glasses and supercooled melts, Rev. Mod. Phys. 75 (2003) 44. https://doi-org.docelec.insa-lyon.fr/10.1103/RevModPhys.75.237.

[95] H.B. Yu, K. Samwer, Y. Wu, W.H. Wang, Correlation between β Relaxation and Self-Diffusion of the Smallest Constituting Atoms in Metallic Glasses, Phys. Rev. Lett. 109 (2012) 095508. https://doi.org/10.1103/PhysRevLett.109.095508.

[96] N. Zou, H.-J. Lu, P.-W. Gu, J.-Y. Wang, X.-K. Feng, J.-Y. Shen, Y.-L. He, L. Li, X.-G. Lu, Thermodynamic assessment and glass forming ability prediction of the Zr-Fe-Cu system, Calphad. 64 (2019) 175–184. https://doi.org/10.1016/j.calphad.2018.12.007.

[97] T. Yamamoto, Y. Yokoyama, T. Ichitsubo, H. Kimura, E. Matsubara, A. Inoue, Precipitation of the ZrCu B2 phase in Zr50Cu50–xAlx (x = 0, 4, 6) metallic glasses by rapidly heating and cooling, J. Mater. Res. 25 (2010) 8. https://doi.org/10.1557/JMR.2010.0105.

[98] H.S. Kim, On the rule of mixtures for the hardness of particle reinforced composites, Materials Science and Engineering: A. 289 (2000) 30–33. https://doi.org/10.1016/S0921-5093(00)00909-6.

[99] A.L. Greer, Partially or fully devitrified alloys for mechanical properties, Materials Science and Engineering: A. 304–306 (2001) 68–72. https://doi.org/10.1016/S0921-5093(00)01449-0.

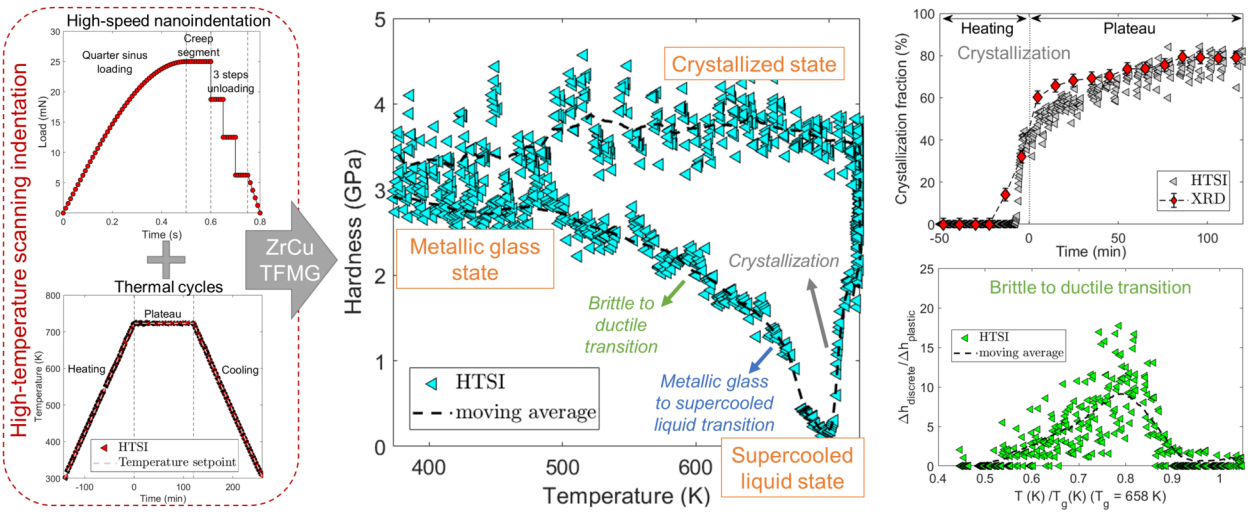
High-temperature scanning indentation
High-speed nanoindentation
Quarter sinus loading
Creep segment
3 steps unloading
Load (mN)
Time (s)
Thermal cycles
Plateau
Heating
Cooling
Temperature (K)
HTSI
Temperature setpoint
Time (min)
ZrCu TFMG
Crystallized state
Metallic glass state
Brittle to ductile transition
Crystallization
Metallic glass to supercooled liquid transition
Supercooled liquid state
HTSI
moving average
Hardness (GPa)
Temperature (K)
Heating
Plateau
Crystallization
Crystallization fraction (%)
HTSI
XRD
Time (min)
Brittle to ductile transition
HTSI
moving average
$\Delta h_{discrete}/\Delta h_{plastic}$
T (K) /T_g(K) (T_g = 658 K)